Two Local FBP Algorithms for Helical Cone-beam Computed Tomography

Hussein Banjak, Marius Costin, Caroline Vienne, Valérie Kaftandjian

Two Local FBP Algorithms for Helical Cone-beam Computed Tomography

Hussein BANJAK [1,2], Marius COSTIN [1], Caroline VIENNE [1], Valérie KAFTANDJIAN [2]

[1] *CEA, Department of Imaging and Simulation for Non-Destructive Testing; Gif-sur-Yvette, France*
Phone: +33169085196; e-mail: hussein.banjak@cea.fr, marius.costin@cea.fr, caroline.vienne@cea.fr
[2] *Laboratory of Vibrations and Acoustics, INSA-Lyon; Villeurbanne, France*
e-mail: valerie.kaftandjian@insa-lyon.fr

Abstract

When dealing with X-ray inspection of large industrial objects, we are generally interested in the 3D reconstruction of a region-of-interest potentially containing flaws or other features rather than on the reconstruction of the whole object. This local reconstruction is related to a reduction in the field-of-view which consequently truncates the projections during data acquisition and produces severe artifacts when using the Feldkamp-Davis-Kress algorithm. To reduce these artifacts caused by transversely truncated projections, we can replace the global ramp filtering approach of the Feldkamp-Davis-Kress method into either the local first derivative operator combined with the Hilbert transform or the 1D Laplace operator followed by a non-local filtering step using a logarithmic kernel. In this paper, our contribution is the extension of the two algorithms from circular to helical scanning geometry. For performance evaluation of our implementations, we present a numerical comparison of the two algorithms with the standard helical FDK algorithm using both complete and truncated data generated by CIVA (the simulation platform for non-destructive testing techniques developed at CEA).

Keywords: helical X-ray computed tomography, region-of-interest, transverse truncations, advanced Feldkamp-Davis-Kress (FDK) algorithm, ramp filter

1. Introduction

During X-ray data acquisition, the obtained projections may be truncated in two basic manners either transversely or axially. It is known that exact reconstruction from truncated projection data is complicated and may even be impossible in certain situations. An efficient solution for handling axial truncation is the use of a helical acquisition trajectory. Accordingly, it is of practical importance to develop a helical cone-beam (CB) reconstruction algorithm that solves also transverse truncation. Different reconstruction algorithms have recently been developed to reduce reconstruction artifacts caused by transversely truncated projections. The most common approach is to extrapolate the truncated projections and then to perform the standard reconstruction from the extrapolated projections [1]. Later, other methods were proposed that do not demand this additional extrapolation step to eliminate truncation artifacts. Algorithms based on the concept of differentiated backprojection (DBP) were proposed [2]. The idea is to compute the derivative of projection data firstly and then to backproject into the image space. Finally, these back-projected differentiated data are filtered along PI-lines using the Hilbert kernel. In this strategy, the derivation and back-projections steps are local and hence not affected by truncation. Thus, reconstruction errors caused by truncation come only from the global filtering step. When projections are truncated, the finite Hilbert transform is not inverted correctly and consequently artifacts appear in the reconstructed image. For a specific point we aim to reconstruct, any truncation in the projection data along the corresponding helix segment will influence the whole reconstruction procedure of this point. Thus, for an exact reconstruction of a considered region, we should find at least one set of non-truncated PI-line segments covering

this region. However, each point inside the helix belongs to one and only one PI-line. Thus, the choice of PI-lines is not flexible and consequently this method does not work well for all types of truncations. As we can see, the main difficulty of this type of algorithms is the inversion of the truncated Hilbert transform. It was demonstrated in [3] that the interior problem does not have a unique solution. Thus, exact and stable reconstruction from truncated projections based on the inversion of the Hilbert transform is generally impossible. However, Kudo et al. [4] stated that a prior knowledge on a small subregion in the object to be reconstructed allows us to obtain a stable inversion of the truncated Hilbert transform. This inversion can be performed in an analytic or iterative way. An efficient technique named POCS (projection into convex sets) [5] originally developed for iterative reconstruction was used by Defrise et al. [6] to invert the truncated Hilbert transform algebraically aided by a prior information on the object. This approach is more costly than analytic ones but yields an accurate reconstruction with several truncation configurations. In summary, if a prior knowledge on a region in the object is available, the inversion of the truncated Hilbert transform is unique and therefore we can obtain an accurate region-of-interest (ROI) reconstruction. However, this type of algorithms is expensive because they are of backprojection-filtration (BPF) structure and based on PI-lines which are time-consuming.

Recently, two interesting filtered-backprojection (FBP) algorithms for ROI reconstruction on circular trajectory have been published [7, 8]. These algorithms are based on the general structure of the FDK algorithm [9] but follow a different approach when filtering the projections. In this work, we present an extension of the two algorithms from circular to helical trajectory. In addition, we show a numerical comparison between the two extended algorithms and the standard FDK algorithm with helical scanning geometry. The paper is organized as follows. In the second section we describe helical scanning geometry and we introduce some standard notations. The classical and modified FDK algorithms for helical reconstruction are also described in this section. In section 3, we show a numerical comparison with both complete and truncated data.

2. Description of the Proposed Algorithms

In this section, we first describe the helical scanning geometry and introduce the different notations used throughout the reconstruction inversion formulas. Then, the steps performed in the FDK algorithm for reconstruction over a helical trajectory are briefly illustrated. Finally, we show two alternative approaches for filtering the projections which can reduce the reconstruction artifacts obtained when the projections are transversely truncated.

2.1. Notations and helical data acquisition geometry

Consider a 3D object of attenuation function $f(\overrightarrow{r})$ where $\overrightarrow{r}$ is the position vector of a point M located in the object. The coordinates of M in the fixed coordinate system of the object $(\overrightarrow{e}_x, \overrightarrow{e}_y, \overrightarrow{e}_z)$ are given by (x,y,z). The actual support of the object is confined within a cylinder of radius r and central axis along the z-direction. Thus, we have

$$f(\overrightarrow{r}) = 0 \qquad \text{for} \qquad x^2 + y^2 > r^2. \tag{1}$$

As illustrated in figure 1, the X-ray source S moves on a helical trajectory of radius R. The coordinates of S in the system $(\overrightarrow{e}_x, \overrightarrow{e}_y, \overrightarrow{e}_z)$ are denoted by

$$\overrightarrow{y}(\lambda) = (R\cos\lambda, R\sin\lambda, h\lambda), \qquad \lambda \in [\lambda_{min}, \lambda_{max}]. \tag{2}$$

Note that λ_{min} and λ_{max} represent the endpoints of the rotation angle λ and $2\pi h$ is the helical pitch (axial translation distance of the source during one complete rotation).

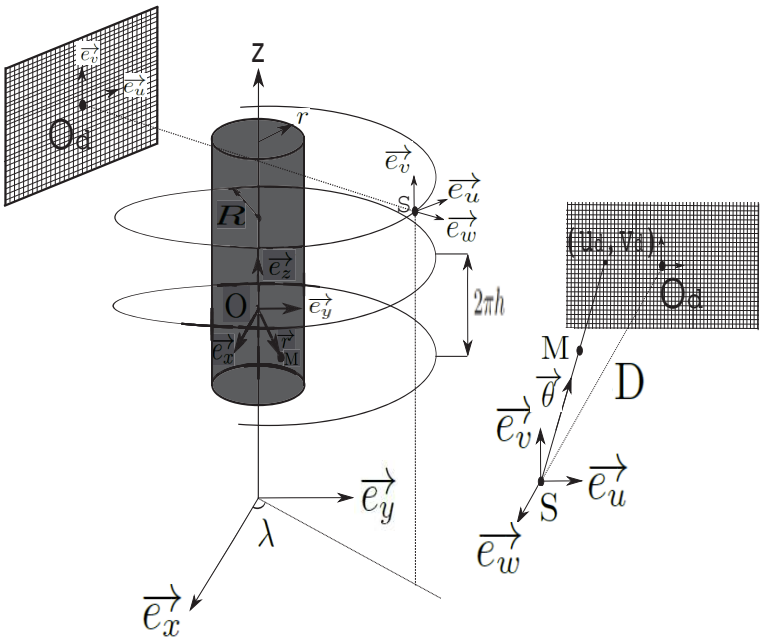

Figure 1. Helical cone-beam acquisition geometry and associated notations.

A planar 2D detector is placed at a distance D from the source with its axes defined by the unit vectors $\overrightarrow{e}_u$ and $\overrightarrow{e}_v$. O_d is the origin of the detector and defined by the orthogonal projection of S onto the detector. The unit vector joining O_d and S is given by $\overrightarrow{e}_w$. The expressions of the three unit vectors $\overrightarrow{e_u}(\lambda)$, $\overrightarrow{e_v}(\lambda)$ and $\overrightarrow{e_w}(\lambda)$ in the coordinate system $(\overrightarrow{e_x}, \overrightarrow{e_y}, \overrightarrow{e_z})$ are:

$$\begin{cases} \overrightarrow{e_u}(\lambda) = (-\sin\lambda)\overrightarrow{e_x} + (\cos\lambda)\overrightarrow{e_y} \\ \overrightarrow{e_v}(\lambda) = \overrightarrow{e_z} \\ \overrightarrow{e_w}(\lambda) = (\cos\lambda)\overrightarrow{e_x} + (\sin\lambda)\overrightarrow{e_y}. \end{cases} \tag{3}$$

Each 3D point $M(x,y,z)$ is projected onto the detector on the pixel of coordinates (u_d, v_d) expressed as:

$$\begin{cases} u_d = D\left(\frac{x\sin\lambda - y\cos\lambda}{x\cos\lambda + y\sin\lambda - R}\right) \\ v_d = -D\left(\frac{z - h\lambda}{x\cos\lambda + y\sin\lambda - R}\right). \end{cases} \tag{4}$$

The measured projection data are given by

$$g(u_d, v_d, \lambda) = \int_{l=0}^{+\infty} f(\overrightarrow{y}(\lambda) + \overrightarrow{\theta}(u_d, v_d, \lambda)l)dl, \tag{5}$$

where $\overrightarrow{\theta}(u_d, v_d, \lambda)$ is the unit vector of the X-ray emitted from the source point S of rotation angle λ and crossing the detector at the point of coordinates (u_d, v_d).

2.2. Standard FDK algorithm

The majority of commercial scanners use the Feldkamp-Davis-Kress (FDK) algorithm due to its simplicity and high efficiency. This algorithm is of filtered-back-projection (FBP) structure which gives an exact reconstruction only in the central plane of the object. The algorithm was developed initially for reconstruction on a circular trajectory [9] and has been later extended by Wang et al. [10] for reconstruction on a helical trajectory. Its inversion reconstruction formula assuming helical trajectory can be expressed as

$$f(\overrightarrow{r}) = \int_{\lambda_i}^{\lambda_f} \frac{RD}{|R - \overrightarrow{r} \cdot \overrightarrow{e_w}(\lambda)|^2} g_F(u_d, v_d, \lambda)\, d\lambda, \tag{6}$$

where $\lambda_i = \frac{z}{h} - \pi$, $\lambda_f = \frac{z}{h} + \pi$ and $g_F(u_d, v_d, \lambda)$ are the filtered data given by

$$g_F(u_d, v_d, \lambda) = \int_{-\infty}^{+\infty} h_r(u_d - u'_d) g'(u'_d, v_d, \lambda)\, du'_d. \tag{7}$$

In this equation, h_r represents the ramp filter kernel and g' refers to the weighted projection data

$$g'(u_d, v_d, \lambda) = \frac{D}{\sqrt{D^2 + u_d^2 + v_d^2}} g(u_d, v_d, \lambda). \tag{8}$$

As we can see, this algorithm consists of three main steps: (a) cosine weighting of the projections (Eq. (8)); (b) row-wise filtering of the weighted projections using the ramp kernel (Eq. (7)); (c) back-projection of the filtered data (Eq. (6)). It should be stated that the ramp filter is global and thus filtering any point in the 2D projection matrix requires a complete knowledge of the whole corresponding detector row. When projections are truncated transversely, this condition is not satisfied and as a result the filtering step is not performed correctly which produces significant artifacts in the reconstructed image.

2.3. FDK algorithm based on the first derivative operator

As we can see in the previous subsection, the error of reconstruction comes only from the ramp filtering step when the projections are truncated transversely. The following fundamental relationship between the ramp filtering and the Hilbert transform was demonstrated in [11]:

$$g_F(u_d, v_d, \lambda) = \frac{1}{2\pi} \frac{\partial}{\partial u_d} g_H(u_d, v_d, \lambda), \tag{9}$$

where g_H is obtained by applying the Hilbert transform along each row in the data matrix g. Based on Eq. (9), Wang et al. [8] have proposed to replace the ramp filter in the standard FDK algorithm on a circular trajectory by the first derivative operator and the Hilbert transform. In this work, we extended this algorithm from circular to helical scanning geometry. This algorithm is based on the FDK method for reconstruction on a helical trajectory but uses an alternative approach of filtering that decomposes the ramp kernel into the first derivative operator and the Hilbert transform. The first derivative is local and gives accurate results even when the projections are truncated whereas the Hilbert transform is global and as a result is affected by truncations. However, when we apply the first derivative operator, we obtain zeros in most of the regions and consequently the filtered data after the Hilbert transform are not influenced significantly by truncations. Thus, the structure of this algorithm is the same as that of the FDK with a different manner of filtering that can handle transverse truncations. Similarly, we first weight the computed projections (Eq. (8)). Then, the weighted datasets are filtered using the first derivative operator and the Hilbert transform(Eq. (9)). Finally, these filtered data are back-projected to get the reconstructed image (Eq. (6)).

2.4. FDK algorithm based on the 1D Laplace operator

Very recently, an important algorithm for circular ROI reconstruction named approximate truncation resistant algorithm for computed tomography (ATRACT) has been published [12]. Similarly, it is based on the FDK algorithm but uses another approach of filtering that decomposes the ramp filter into the 2D Laplace operator coupled with a 2D Radon-based filtering operation.

This algorithm is very efficient and gives artifact-free reconstructions when the projections are truncated transversely. The only drawback of this algorithm is the high computational cost of the 2D Radon-based filtering step. Later, Xia et al. [7] optimized this algorithm by proposing another approach that replaces the ramp filter by the 1D Laplace operator and a 1D logarithmic-based filtering step. An analytical proof of the algorithm was illustrated in [13]. Briefly, the ramp kernel in the Fourier domain $|\sigma|$ can be reformulated as follows:

$$\begin{aligned} |\sigma| &= \sigma\,\mathrm{sgn}(\sigma) \\ &= (2\pi i\sigma)^2 \left(-\frac{1}{4\pi^2}\frac{\mathrm{sgn}(\sigma)}{\sigma}\right). \end{aligned} \tag{10}$$

The first term in Eqn. (10) corresponds to the Fourier transform of the 1D Laplace operator and the second term represents the Fourier transform of the logarithmic kernel. Knowing that multiplication in the Fourier domain refers to convolution in the spatial domain, the ramp-filtered data g_F can be computed as

$$g_F(u_d, v_d, \lambda) = -\frac{1}{4\pi^2}\int_{-\infty}^{+\infty} \ln|u_d - u'_d|\, g_L(u'_d, v_d, \lambda)\, du'_d, \tag{11}$$

where g_L are the Laplace filtered data defined by

$$g_L(\lambda, u_d, v_d) = \frac{\partial^2}{\partial u_d^2} g'(\lambda, u_d, v_d). \tag{12}$$

Remind that g' are the cosine weighted projections defined previously in Eqn. (8). Thus, the ramp filter is mathematically identical to the Laplace operation (Eqn. (12)) and a 1D logarithmic-based filtering step (Eqn. (11)). The Laplace operation is local and hence is not influenced by truncations whereas the 1D logarithmic-based filtering is global but less sensitive to truncations compared to the 1D ramp filtering step. Note that this algorithm was also developed for reconstruction on circular trajectory. Similarly, our main contribution was to adapt it for helical scanning geometry using the same approach which was followed during the extension of the standard FDK algorithm from circular to helical trajectory.

3. Results and Numerical Comparison

We present in this section a numerical comparison of the mentioned algorithms from both truncated and non-truncated data. CIVA software [14] was used to carry on numerical simulations and evaluate the performance of the developed algorithms. Table 1 indicates the configuration used when simulating the cone-beam helical projections.

Table 1. Numerical simulation parameters.

Object radius (r)	7.5 mm
Helix radius (R)	30 mm
Source-detector distance (D)	60 mm
Helical pitch (2πh)	2.3125 mm
Number of projections per turn	360
Detector pixel size	0.065×0.065 mm^2
Detector sampling	100×512 pixels
Reconstruction matrix	$600 \times 600 \times 600$ voxels

Our simulated object is a computer-aided-design (CAD) model phantom which is similar to the Defrise disk phantom with additional rectangular and circular holes of different sizes. The

height of this phantom is 18.5 mm and consists of five circular disks with thickness 2.5 mm stacked along the z-direction and separated by 1.5 mm. The radius of each disk is 7.5 mm and the values of the diameter of each circular hole and the edge of each square hole are given in mm as follow: 1.0, 0.8, 0.6, 0.5, 0.4, 0.3, 0.2, 0.1, 0.05 and 0.025. The phantom is made of polymethyl-methacrylate (PMMA) and we used monochromatic X-ray source of 80 KeV. Figure 2 shows the reconstruction of the phantom using the three algorithms described in Section 2 with complete and noise-free projections. The reconstruction results are similar and it is clear that the reconstructed and true values along the 1D profile are in good agreement for the three algorithms.

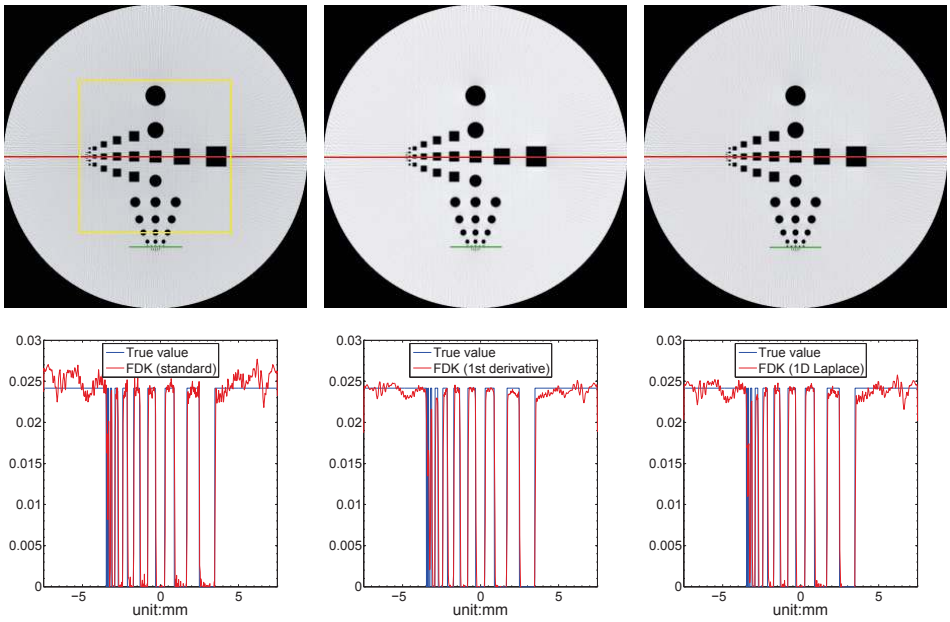

Figure 2. Reconstruction of the disk phantom using the three mentioned algorithms with a display window [0,0.03]. The first column corresponds to the standard FDK reconstruction whereas the second and third columns refer to reconstruction results using the modified FDK algorithms which are based on the first derivative operator and the 1D Laplace operator, respectively. The horizontal central slice of each reconstructed image is displayed in the first row with the red lines used for the 1D numerical comparison plotted in the second row.

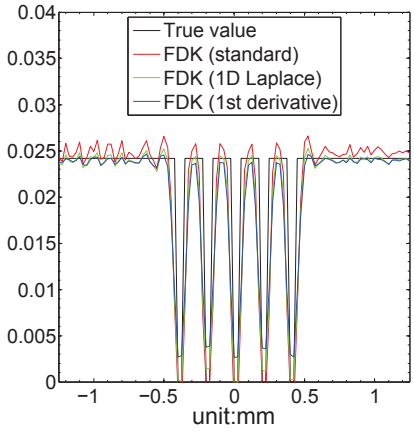

Figure 3. Evaluation of the spatial resolution using a 1D numerical comparison along the green lines illustrated in figure 2.

For a theoretical analysis of the spatial resolution, the type of the filter kernel for each algorithm should be studied. Referring to the frequency response of each filter, we notice that the ramp kernel and the second derivative operator are high-pass filters whereas the first derivative operator is a band-pass filter. Thus, the modified FDK algorithm based on the first derivative

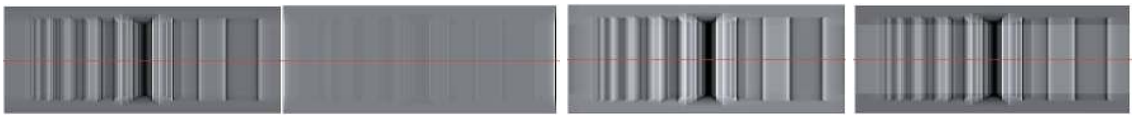

(a) FDK (complete data) (b) FDK (truncated data) (c) FDK$^{(1)}$ (truncated data) (d) FDK$^{(2)}$ (truncated data)

Figure 4. Comparison of one projection of the 3D sinogram filtered by the three described algorithms where FDK$^{(1)}$ and FDK$^{(2)}$ correspond to FDK based on the first derivative operator and the 1D Laplace operator, respectively.

operator is supposed to denote a poor spatial resolution compared with the other two algorithms. For numerical evaluation, we show in figure 3 a 1D numerical comparison along the circular holes of diameter value 0.05 mm (green lines illustrated in figure 2). The standard FDK algorithm and the FDK algorithm based on the 1D Laplace operator reconstructions show good spatial resolution whereas the FDK algorithm based on the first derivative operator shows a slight loss in the spatial resolution.

To study reconstruction with truncated data, 128 pixels on each side of every row in the detector are set to zero. Within this configuration, only half of the object is viewed by the detector and as a result the field-of-view (FOV) is reduced to its half size. In order to compare the impact of each filtering approach on truncated data, we represent in figure 4 2D projections obtained in the 3D sinogram filtered using the three mentioned algorithms. Figure 4a is the reference in our numerical comparisons and shows a filtered 2D projection obtained from complete data using the standard FDK algorithm. Figures 4b, 4c and 4d illustrate filtered 2D projections obtained from truncated data using FDK, FDK$^{(1)}$ and FDK$^{(2)}$, respectively. It is obvious that the filtering steps of FDK$^{(1)}$ (figure 4c) and FDK$^{(2)}$ (figure 4d) are local in contrast to the ramp filter of the standard FDK algorithm that denotes a filtered sinogram (figure 4b) far from the reference (figure 4a). Figure 5 represents the horizontal central slices in the FOV (yellow square region in figure 2) of the images reconstructed by the three algorithms with a 1D numerical comparison along the red lines. The first column corresponds to the standard FDK reconstruction whereas the second and third columns correspond to FDK$^{(1)}$ (modified FDK algorithm based on the first derivative operator) and FDK$^{(2)}$ (modified FDK algorithm based on the 1D Laplace operator), respectively. As we can see, the standard FDK algorithm can not handle transverse truncation and severe distortions (cup artifacts) appear in the reconstructed image. On the other hand, the two modified algorithms show reconstructions free of artifacts. The 1D profile comparison demonstrates that an important reconstruction offset appears with the standard FDK algorithm in case of truncated data whereas this offset can be suppressed by using the two modified FDK algorithms. It should be mentioned that for these two modified FDK algorithms a min-max scaling method was applied manually after reconstruction [13]. Without this step, the reconstruction suffers from a global scaling issue and the measured values are not quantitative. The final calibrated reconstructed values $f_c(i)$ are given by

$$f_c(i) = \frac{(f_r(i) - f_{r(min)})(f_{max} - f_{min})}{(f_{r(max)} - f_{r(min)})} + f_{min}, \tag{13}$$

where $f_{r(min)}$ and $f_{r(max)}$ are the minimum and maximum values in the reconstructed image f_r, respectively, while f_{min} and f_{max} correspond to the minimum and maximum attenuation values in the FOV of the original object, respectively. The mean square error (MSE) metric is used to assess the reconstructed image quantitatively:

$$MSE(f_r) = \frac{1}{N}\sum_{i=1}^{N} |f_r(i) - f(i)|^2, \tag{14}$$

where N is the total number of voxels in the original image f and its reconstructed one f_r.

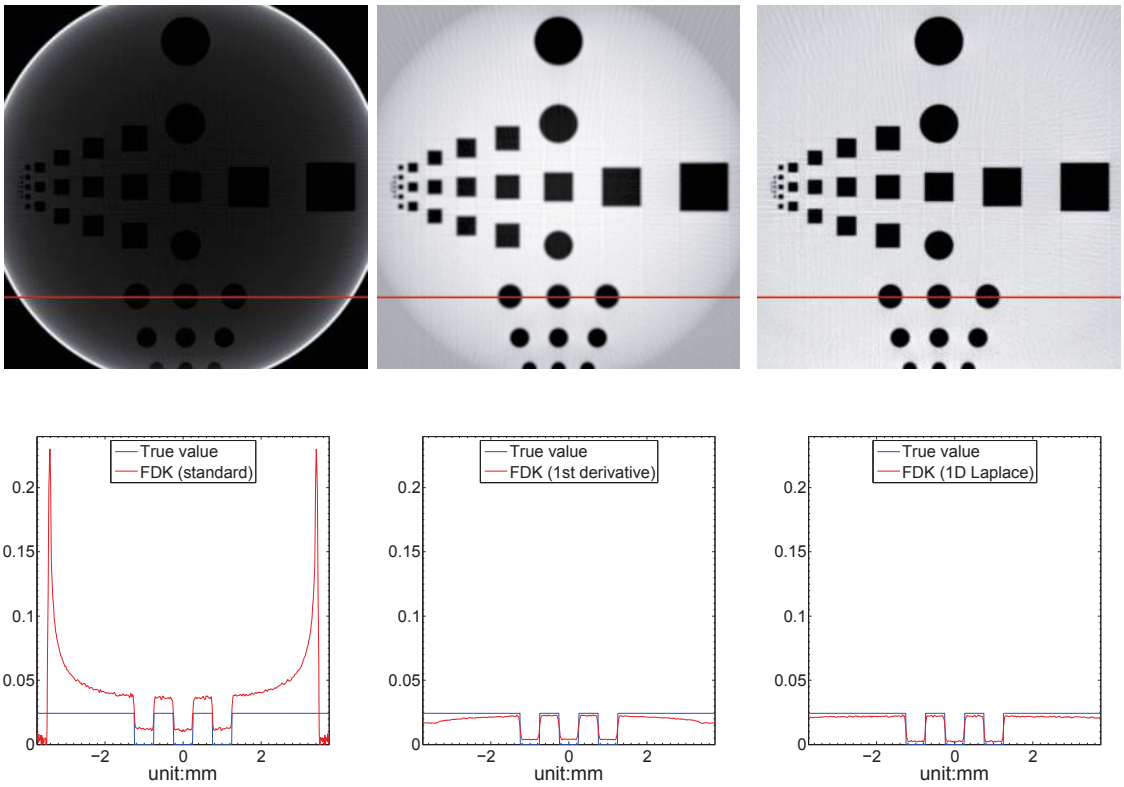

Figure 5. FOV reconstruction in case of truncated data with the red lines used for 1D numerical comparison.

Table 2 shows a comparison of the three algorithms for the first (complete data) and the second (truncated data) simulations. In this table, we show the measured MSE and the time of reconstruction for each algorithm. The MSE is computed on the whole 3D volume in the case of complete data and only for the considered FOV when the projections are truncated.

Table 2. Numerical comparison of the three described algorithms with both complete and truncated data.

Reconstruction algorithm	FDK	FDK$^{(1)}$	FDK$^{(2)}$
Reconstruction time (minutes)	61.5	61.4	63.5
Mean-square-error (complete data) $\times 10^{-6}$	5	6	6
Mean-square-error (truncated data) $\times 10^{-6}$	448	7	6

4. Conclusions

In this work, two ROI reconstruction algorithms for circular scanning geometry were extended to helical trajectory. For performance evaluation, we illustrated a numerical comparison of the two extended algorithms and the standard helical FDK algorithm. Our computer simulations show reconstructions with both complete and transversely truncated data. There is no observable difference between the image quality of reconstructions from complete data with the three described algorithms. However, when the projections are truncated transversely, the two modified FDK algorithms perform better than the standard one that uses the global ramp filter. In particular, these two algorithms solve the well-known cup artifacts usually observed with the standard FDK algorithm in the case of truncated data. In terms of performance, the reconstruction time is similar for the three mentioned algorithms. It should be noted that these two local reconstruction algorithms are of great interest because of their filtered-backprojection structure and consequently they are not time-consuming like backprojection-filtration and PI-line based algorithms or other iterative methods for local reconstruction.

Acknowledgements

This work was performed within the framework of the Labex CeLyA of Université de Lyon, operated by the French National Research Agency (ANR-10-LABX-0060/ANR-11-IDEX-0007).

References

1. B Ohnesorge, T Flohr, K Schwarz, J Heiken, and K Bae, 'Efficient correction for ct image artifacts caused by objects extending outside the scan field of view', Medical physics, Vol 27, No 1, pp 39-46, 2000.
2. Y Zou and X Pan, 'Exact image reconstruction on pi-lines from minimum data in helical cone-beam ct', Physics in Medicine and Biology, Vol 49, No 6, pp 941, 2004.
3. F Natterer, The mathematics of computerized tomography, Vol 32. Siam, 1986.
4. H Kudo, M Courdurier, F Noo, and M Defrise, 'Tiny a priori knowledge solves the interior problem in computed tomography', Physics in medicine and biology, Vol 53, No 9, pp 2207, 2008.
5. D C Youla and H Webb, 'Image restoration by the method of convex projections: Part 1theory', Medical Imaging, IEEE Transactions on, Vol 1, No 2, pp 81-94, 1982.
6. M Defrise, F Noo, R Clackdoyle, and H Kudo, 'Truncated hilbert transform and image reconstruction from limited tomographic data', Inverse problems, Vol 22, No 3, pp 1037, 2006.
7. Y Xia, A Maier, H G Hofmann, F Dennerlein, K Mueller, and J Hornegger, 'Reconstruction from truncated projections in cone-beam ct using an efficient 1d filtering', in SPIE Medical Imaging, pp 86681C-86681C, International Society for Optics and Photonics, 2013.
8. X-C Wang, B Yan, L Li, and G-E Hu, 'Cone-beam local reconstruction based on a radon inversion transformation', Chinese Physics B, Vol 21, No 11, pp 8702, 2012.
9. L Feldkamp, L Davis, and J Kress, 'Practical cone-beam algorithm', JOSA A, Vol 1, No 6, pp 612-619, 1984.
10. G Wang, T-H Lin, P-C Cheng, and D M Shinozaki, 'A general cone-beam reconstruction algorithm', Medical Imaging, IEEE Transactions on, Vol 12, No 3, pp 486-496, 1993.
11. F Noo, M Defrise, R Clackdoyle, and H Kudo, 'Image reconstruction from fan-beam projections on less than a short scan', Physics in Medicine and Biology, Vol 47, No 14, pp 2525, 2002.
12. F Dennerlein and A Maier, 'Approximate truncation robust computed tomographyatract', Physics in medicine and biology, Vol 58, No 17, pp 6133, 2013.
13. Y Xia, F Dennerlein, S Bauer, H Hofmann, J Hornegger, and A Maier, 'Scaling calibration in region of interest reconstruction with the 1d and 2d atract algorithm', International journal of computer assisted radiology and surgery, Vol 9, No 3, pp 345-356, 2014.
14. R Fernandez, M Costin, D Tisseur, A Leveque, and S Legoupil, 'Civa computed tomography modeling', at WCNDT, 2012.